

1 **Shock and Static Pressure Demagnetization of Pyrrhotite and Implications for**
2 **the Martian Crust**

3
4
5 Karin L. Louzada^{1*}, Sarah T. Stewart¹, Benjamin P. Weiss², Jérôme Gattacceca³, Natalia S.
6 Bezaeva⁴

7
8 ¹Department of Earth and Planetary Sciences, Harvard University, 20 Oxford Street, Cambridge,
9 MA 02138, USA

10 ²Department of Earth, Atmospheric and Planetary Sciences, Massachusetts Institute of
11 Technology 54-814, 77 Massachusetts Avenue, Cambridge, MA 02139, USA

12 ³Department of Geophysics and Planetology, CEREGE (CNRS, Aix-Marseille University), BP
13 80, 13545 Aix en Provence Cedex 4, France

14 ⁴Earth Physics Department, Faculty of Physics, M.V. Lomonosov Moscow State University,
15 Leninskie gory, 119991, Moscow, Russia

16
17 *louzada@post.harvard.edu

18
19
20 *Submitted to EPSL – July 10, 2009*

21 **Abstract**

22 Mars no longer possesses a global magnetic field of internal origin. However, strong crustal
23 magnetic fields suggest that it did in the past. Over large impact basins, the demagnetization of
24 the crust by low shock pressures of a few GPa has been inferred from the absence of crustal
25 magnetization. Attempts to understand the impact demagnetization process and to infer the
26 magnetic properties (e.g., carrier phase) of the Martian crust have been based on the
27 experimental pressure demagnetization of magnetic rocks and minerals. We investigate the
28 magnitude of demagnetization and permanent changes in the intrinsic magnetic properties, of
29 single and multidomain natural pyrrhotite under hydrostatic pressures up to 1.24-1.8 GPa and
30 shock pressures up to 12 GPa. Both static and dynamic pressures result in an irreversible loss of
31 predominantly low coercivity magnetic remanence. The pressure demagnetization results can be
32 divided into a low pressure regime and a high pressure regime. The transition between the two
33 regimes roughly corresponds to the ferri- to paramagnetic transition and the Hugoniot Elastic
34 Limit (~3.5 GPa) of pyrrhotite. It is unknown at present whether these transitions are related. The
35 low pressure regime is characterized by a decrease in remanence with increasing pressure in both
36 static and shock experiments. The higher pressure regime, probed only by shock experiments, is
37 characterized by a more complicated modification of remanence as a result of permanent
38 changes in the intrinsic magnetic properties of the material. These changes include an increase in
39 saturation remanence and a change in the coercivity distribution towards greater bulk coercivity.
40 Samples that were only submitted to hydrostatic pressure up to 1.24-1.8 GPa do not show
41 permanent changes in the magnetic properties. Demagnetization of pyrrhotite as a result of
42 pressure is likely due to a combination of domain reordering (in multidomain grains) and
43 magnetostrictive effects (in single-domain grains). Microfracturing of multidomain grains
44 effectively reduces the domain-size leading to the observed increase in single-domain like
45 behavior. The pressure effects seen in this study generally hold for all magnetic phases. The
46 pressure demagnetization results for pyrrhotite suggest that it is a possible carrier of the
47 magnetization in the Martian crust.

48 1. Introduction

49 Mars no longer possesses a global magnetic field. However, the presence of crustal magnetic
50 fields observed by the NASA Mars Global Surveyor spacecraft (Acuña et al., 1999; Lillis et al.,
51 2004; 2008b) and the identification of magnetization in Martian meteorites (Antretter and Fuller,
52 2002; Gattacceca and Rochette, 2004; Weiss et al., 2002; 2008) suggests that it did in the past.
53 The majority of the crustal magnetic anomalies are located in the heavily cratered southern
54 hemisphere and the intensities of the magnetic anomalies at altitude are up to ~20 times greater
55 than terrestrial anomalies at similar altitudes (Acuña et al., 1999; Langel et al., 1982). Either the
56 intensity of the magnetic field was much greater on Mars in the past than it is on the Earth
57 presently or the basaltic Martian crust is enriched in magnetic minerals compared to the Earth's
58 crust. Recent paleointensity studies of ALH84001 favor the latter scenario (Gattacceca and
59 Rochette, 2004; Weiss et al., 2008). Furthermore, large regions of crust devoid of magnetization
60 above and around the youngest impact basins (Hellas, Argyre and Isidis) suggest that impact
61 demagnetization has played an important role in shaping the crustal magnetic field of Mars.

62 Impact cratering may affect the magnetic remanence of crustal rocks in the following ways.
63 Near the impact point, the impact energy leads to melting of the projectile and target, producing
64 a melt sheet lining the basin floor. In the presence of an ambient magnetic field, the melt sheet
65 can acquire a thermoremanent magnetization. The fact that the centers of the youngest Martian
66 impact basins are devoid of crustal magnetic anomalies has been taken as evidence of cessation
67 of the global magnetic field ~4 Ga (Lillis et al., 2008a) based on crater count age estimates (Frey,
68 2008). Outside of the basins, shock pressure decays to levels where heating from the impact is
69 not an important demagnetization mechanism (a few GPa) and nonthermal processes dominate
70 the shock modification of rocks and minerals.

71 In the absence of an ambient magnetic field, the crust may (partially) demagnetize as a result
72 of shock. However, in the presence of an ambient planetary or strong crustal magnetic field, a
73 shock remanent magnetization may be acquired as well. Explosive shock experiments on igneous
74 rocks in the Earth's magnetic field indicate that shock remanent magnetization is less efficient
75 than thermoremanent magnetization and that it may be susceptible to viscous decay over
76 geologic time (Gattacceca et al., 2007a). Paleomagnetic evidence of shock remanent
77 magnetization in naturally shocked basalts at Lonar crater, India (<50 ka), has been obscured by
78 viscous processes (Louzada et al., 2008). In this study we will only focus on the process of
79 demagnetization by pressure.

80 Estimates of the amplitude of the pressures responsible for demagnetization on Mars are
81 based on calculated spatial distributions of shock pressure and spacecraft observations of the
82 distribution of crustal magnetization around impact basins. Preliminary pressure estimates for
83 partial demagnetization around Hellas basin are low, on the order of a few GPa (Hood et al.,
84 2003; Kletetschka et al., 2004; Mohit and Arkani-Hamed, 2004). However, accurate
85 determination of the demagnetizing pressures is sensitive to the poorly constrained impact
86 conditions that lead to the formation of basins, the radius of curvature of the planet, wave-
87 interference in the crust, and the crust-mantle boundary (Louzada and Stewart, in press). Over
88 Hellas, azimuthally averaged magnetic field profiles suggest that the crust has been completely
89 demagnetized at distances up to 0.8 basin radii (~920 km) and partially demagnetized out to ~1.4
90 basin radii (~1650 km) (Mohit and Arkani-Hamed, 2004). Considering the uncertainties in basin
91 formation listed above, for Hellas, complete demagnetization is estimated to occur between 1.1
92 and 3.4 GPa (Louzada and Stewart, in press).

93 One potential carrier of the crustal magnetization on Mars is pyrrhotite. Pyrrhotite (an iron
94 sulfide) is present in all subclasses of Martian meteorites. It is a common phase in the lherzolithic
95 shergottites (McSween Jr and Treiman, 1998 and references therein). Pyrrhotite is also the
96 principal magnetic carrier in the basaltic shergottites (Collinson, 1986; Rochette et al., 2001;
97 2005), which are thought to be representative of the Martian crust (Longhi et al., 1992).

98 Limited pressure demagnetization experiments have been conducted on pyrrhotite. Under
99 hydrostatic pressures, saturation isothermal remanent magnetization in pyrrhotite has been
100 shown to demagnetize by ~16% in a pyrrhotite-bearing shergottite at 1.24 GPa (Bezaeva et al.,
101 2007) and completely in pure pyrrhotite at 3 GPa (e.g., Rochette et al., 2003). Caution must be
102 used when comparing these hydrostatic results to shock-induced demagnetization and
103 extrapolating to planetary impact cratering. Neither dynamic nor static experiments can
104 reproduce the strain-rate and stress duration conditions that occur during planetary-scale impact
105 cratering. If pressure demagnetization is sensitive to kinetic processes, or directed stress rather
106 than hydrostatic pressure, then the results of the static and dynamic studies will be different.
107 Furthermore, each shocked sample undergoes a different pressure loading and unloading path
108 that depends on the achieved shock state.

109 In this study, we investigate the response of natural pyrrhotite samples to shock pressures up
110 to 12 GPa and hydrostatic pressures up to 1.8 GPa. We report on the magnitude of
111 demagnetization, differences between shock and static experimental results, and permanent
112 changes in the intrinsic magnetic properties of pyrrhotite. We explore the mechanisms
113 responsible for the observed changes and discuss the implications for planetary crustal
114 magnetization.

115

116 2. Methods

117 We performed hydrostatic and shock recovery experiments on three natural pyrrhotite
118 samples: (1) a ~1 cm diameter smooth rounded pure pyrrhotite nodule (No. 98080) from
119 Sudbury, Canada, (2) a euhedral single-crystal (~3×5×1 cm) of pure pyrrhotite with hexagonal
120 habitus and smooth crystal faces (No. 127037) from Chihuahua, Mexico, and (3) a pyrrhotite-
121 bearing metamorphic schist from the Wilson Terrane (Antarctica). In order to determine the
122 changes in remanence and other magnetic properties as a result of pressure, a suite of (magnetic)
123 characterization experiments (Table 1) were conducted on selected samples before and after
124 stress application. Shock experiments on the pure samples (1 and 2) have been briefly discussed
125 in Louzada et al. (2007); the schist (3) has been previously studied in explosive shock
126 experiments up to 30 GPa (Gattacceca et al., 2007b).

127 2.1 Sample characterization

128 Pyrrhotite (Fe_{1-x}S , $0 < x < 0.125$) owes its magnetic properties to vacancy ordering in a NiAs
129 crystal structure. When the vacancies are arranged on a superstructure such that alternating layers
130 ($00l$) contain an unequal number of iron atoms, pyrrhotite (Fe_7S_8) exhibits monoclinic symmetry
131 and is ferrimagnetic (Bertaut, 1953) with a strong basal-plane magnetic anisotropy. Other
132 vacancy distributions result in hexagonal symmetry (Fleet, 1968; Morimoto et al., 1975) and
133 usually result in antiferromagnetic behavior. Natural pyrrhotite commonly contains intergrowths
134 of both antiferromagnetic hexagonal and ferrimagnetic monoclinic pyrrhotite (Morimoto et al.,
135 1975).

136 The presence of (monoclinic) pyrrhotite was confirmed in both the single-crystal and the
 137 nodule by temperature cycling (Figure S1) through a magnetic transition at 30 K (Rochette et al.,
 138 1990), X-ray diffraction (Table S1) and chemical compositional analyses (Table S2). In the
 139 schist, the presence of monoclinic pyrrhotite was confirmed by its Curie temperature (Gattacceca
 140 et al., 2007b). Uncompressed (hexagonal) lattice parameters, a and c , are 6.857 ± 0.006 and
 141 22.89 ± 0.06 Å in the nodule and 6.846 ± 0.033 Å and 22.84 ± 0.23 Å in the single-crystal,
 142 respectively, consistent with previous studies on pyrrhotite (Dekkers, 1988; Nkoma and Ekosse,
 143 1999). In all specimens, the maximum peak intensity in the X-ray diffraction patterns occurs for
 144 the (208) plane, indicative of pyrrhotite. In the single-crystal, a doublet occurs with peaks located
 145 at 2.0473 and 2.0615 Å (Figure S2), indicative of monoclinic pyrrhotite (Yund and Hall, 1969).
 146 Based on Fe/S ratios (Table S2) the single-crystal (0.876 ± 0.01) is enriched in monoclinic
 147 pyrrhotite (Fe/S = 0.875) with respect to the nodule (0.893 ± 0.01).

148 Magnetic hysteresis measurements (Table S3) can provide insight into the domain-size of the
 149 magnetic fractions. The theoretical ratio of the saturation remanence in zero field, M_{rs} , to the in-
 150 field saturation magnetization, M_s , in single-domain (SD, <1.5 - 2 µm; Menyeh and O'Reilly,
 151 1991; Soffel, 1977) pyrrhotite with triaxial anisotropy confined to the basal plane, is 0.75
 152 (Dunlop and Özdemir, 1997, p.321); although measured values are generally lower than this
 153 prediction. Wasp-waisted hysteresis loops indicate a distribution of coercivities (e.g., Dunlop and
 154 Özdemir, 1997, p. 316) and strong paramagnetic signals at high fields indicate that the nodule
 155 also contains a significant superparamagnetic (SP) fraction. M_{rs}/M_s is much lower ($0.1479 \pm$
 156 0.004) in the single-crystal, indicative of multidomain (MD) grains (>40 µm; Dekkers, 1988).
 157 The presence of superparamagnetic fractions in both pure samples is independently confirmed by
 158 a slight increase in remanence below 25 K in low-temperature cycling measurements (Figure S1;
 159 Rochette et al., 1990). Based on hysteresis parameters ($M_{rs}/M_s = 0.499 \pm 0.028$ and $B_{cr}/B_c = 1.29$
 160 ± 0.12 , where B_{cr} and B_c are the coercivity of remanence and the bulk coercive force,
 161 respectively), the pyrrhotite grains in the schist are pseudo-single-domain (PSD) (Gattacceca et
 162 al., 2007b).

163 The strong basal-plane magnetic anisotropy of pyrrhotite is evident in the orientation
 164 dependant shapes of the hysteresis loops (Figure S3). Due to nonlinearity of susceptibility
 165 (Hrouda, 2007), low-field anisotropy of magnetic susceptibility in pyrrhotite is field and
 166 frequency dependant (Martín-Hernández et al., 2008, and references therein). Anisotropy of
 167 magnetic susceptibility (Table S4) was determined from the slopes fit to hysteresis loops
 168 between -2.5 and 2.5 mT (full range -1 to +1 T) in 12 directions. The low-field slopes were then
 169 fitted to a second-rank tensor to determine the susceptibility ellipsoid (Jelínek, 1973). The
 170 anisotropy degree, P , the ratio of the maximum to minimum principal susceptibilities (κ_1/κ_3) and
 171 a measure of the magnitude of anisotropy, is very high in the pure pyrrhotite samples (45.98 in
 172 the SD/SP nodule and 56.24 in the MD single-crystal). High anisotropy degrees have also been
 173 reported in other single-crystal pyrrhotite samples by Martín-Hernández et al. (2008). The shape
 174 of the susceptibility ellipsoid is described by the shape factor, $T = 2 \left[\ln(\kappa_2/\kappa_3) / \ln(\kappa_1/\kappa_3) \right] - 1$.
 175 Since the magnetization is confined to the basal plane, the magnetic fabric in pyrrhotite might be
 176 expected to be planar with an oblate susceptibility ellipsoid ($0 < T < 1$) in a single crystal, as it is in
 177 the unshocked MD sample ($T = 0.697$, Figure S3). On the other hand, the susceptibility ellipsoid
 178 of the unshocked SD/SP nodule is prolate ($T = -0.776$), indicating a linear magnetic fabric.
 179 Oblate, prolate and neutral ($T \sim 0$) ellipsoids have in fact been observed in other natural
 180 pyrrhotites (Martín-Hernández et al., 2008). Anisotropy of magnetic susceptibility of the PSD

181 pyrrhotite-bearing schist is much smaller ($P = 1.741$), within the range of previous measurements
 182 on schists (e.g., Hrouda, 2007) and is oblate ($T = 0.697$) as would be expected if the pyrrhotite
 183 grains grew with their basal-plane (001) parallel to the foliation in the rock.

184 Other sample characterization measurements include: (1) uncompressed density, (2)
 185 longitudinal and shear sound speeds, (3) acquisition and alternating field (AF) demagnetization
 186 of isothermal remanent magnetization in order to discover changes in the distribution of
 187 coercivity fractions, and (4) Bitter (1931) imaging and magnetic force microscopy (Digital
 188 Instruments NANOSCOPE III at Institute of Rock Magnetism, University of Minnesota) to
 189 image the magnetic domain sizes and shapes. Rock-magnetic measurements were performed on
 190 2G Enterprises super-conducting magnetometers with automated sample changers in the
 191 paleomagnetic laboratories at the California Institute of Technology, the Massachusetts Institute
 192 of Technology, Yale University, and CEREGE, France, with a sensitivity of 10^{-12} Am^2 . The
 193 samples in this study generally have magnetizations of 10^{-7} - 10^{-4} Am^2 .

194 2.2 Planar shock recovery experiments

195 Shock recovery experiments were conducted in the ambient laboratory magnetic field (12.7
 196 μT directed up-range) on disc-shaped ($\sim 3 \text{ mm}$ diameter, $\sim 1 \text{ mm}$ tall) single-crystal and nodule
 197 specimens, and ($\sim 12 \text{ mm}$ diameter, $\sim 1 \text{ mm}$ tall) schist specimens at pressures up to 12 GPa
 198 (Table 2). A subset of the data have been discussed in Louzada et al. (2007). Prior to shock
 199 demagnetization, isothermal remanence was acquired in magnetic fields of 390 to 1100 mT,
 200 which resulted in (near-) saturation of the specimens. Six specimens of the SD/SP nodule were
 201 cored from two subparallel slices cut in a random orientation, resulting in a ~ 14 - 30° angle
 202 between the plane of the disc and the easy-plane of magnetization. Nine specimens of the MD
 203 single-crystal were cut from two roughly perpendicular slices resulting in saturation remanence
 204 at angles of $<10^\circ$ or $>80^\circ$ with the plane of the disc. Four specimens of the PSD schist were
 205 cored parallel or perpendicular to the metamorphic foliation, the magnetization in each of the
 206 samples made an angle of 44 - 48° with the plane of the disc.

207 Shock was induced by aluminum (Al6061) flyer plates (34 to 38 mm in diameter and 3 mm
 208 thick) atop ~ 75 -mm long polycarbonate sabots that were accelerated to 180-1250 m/s using
 209 compressed helium in the 40-mm horizontal, single-stage gas-gun in the Shock Compression
 210 Laboratory at Harvard University (Stewart, 2004). The magnetic specimens were embedded in
 211 aluminum capsules (6-20 mm in diameter and 9-19 mm tall). The capsules have a minimal affect
 212 on the magnetic measurements; in the lowest moment samples (schists) only 5.1-9.7% of
 213 saturation isothermal remanence is attributed to the aluminum. The cylindrical symmetry of the
 214 target assembly and lateral and rear momentum traps (Figure 1) ensure that the wave profiles in
 215 the specimens are planar with minimal interference from reflections. Simulations of the
 216 experiments using the shock physics code CTH (McGlaun et al., 1990) indicate that ~ 94 vol% of
 217 the specimens experience the calculated peak shock pressure within $\pm 0.5 \text{ GPa}$ (Figure S4).

218 Peak shock pressure (principal stress, σ_1) in the specimen is determined using the impedance
 219 match solution (Melosh, 1989, p. 54-57) and the material shock parameters in Table S5. In
 220 elastic solids, the longitudinal (principal) stress wave is accompanied by two orthogonal,
 221 transverse stress waves of lower amplitude (σ_2 and σ_3 , $\sigma_2 = \sigma_3$). The average pressure, P , in the
 222 specimen is: $P = \frac{1}{3}(\sigma_1 + 2\sigma_2) = \frac{1}{3}\sigma_1(1 + \nu)/(1 - \nu)$. The dimensionless Poisson's ratio, ν , can be
 223 determined from the longitudinal sound speed (c_p) and shear wave speed (c_s) (Table 2) using the

224 following relationship: $\nu = \left[1/2(c_p / c_s)^2 - 1 \right] / \left[(c_p / c_s)^2 - 1 \right]$. As average pressure increases, the
 225 difference between the longitudinal and transverse stresses increases until the Hugoniot Elastic
 226 Limit is reached, and the shear stress $[\tau = (\sigma_1 - \sigma_2)/2]$ no longer increases. When the Hugoniot
 227 Elastic Limit is exceeded, both elastic and plastic deformation take place. For strong pressure
 228 waves, the difference between the longitudinal and transverse stresses is small compared to the
 229 mean stress and $P \sim \sigma_1$. We performed laser velocity interferometer experiments on the MD
 230 single-crystal and determined a Hugoniot Elastic Limit of ~ 3.5 GPa for pyrrhotite (Figure S5),
 231 comparable to that of basalt (e.g., 2 GPa; Sekine et al., 2008).

232 2.3 Hydrostatic pressure demagnetization experiments

233 Hydrostatic pressure demagnetization of saturation isothermal remanence acquired in a >3 T
 234 field was conducted on one specimen of the MD single-crystal (No. 127037) using a
 235 nonmagnetic (“Russian” Ni₅₇Cr₄₀Al₃/ Ti-alloy) composite high pressure cell of piston-cylinder
 236 type (Sadykov et al., 2008) up to 1.24 GPa and one specimen of the SD/SP nodule (No. 98080)
 237 up to 1.8 GPa using a similar composite pressure cell. Pressure experiments on the schist are
 238 reported in Bezaeva et al. (submitted). The advantage of experiments using these cells is that the
 239 small size (outer diameter ~ 30 mm) allows it to be placed inside a 2G Enterprises SQUID
 240 magnetometer so that remanence measurements can be made while under pressure as well as
 241 upon decompression. Hydrostatic compression up to 1.24 or 1.8 GPa (depending on the
 242 operating pressure limit of the cell used) was applied in a near zero magnetic field ($<5\mu\text{T}$) to
 243 avoid acquisition of a piezo-remanent magnetization. As a transmitting-pressure medium, we
 244 used the inert polyethylsiloxane (PES-1) liquid (Kirichenko et al., 2005).

245

246 3. Results

247 3.1 Pressure demagnetization

248 Both dynamic (Table 2) and static (Table 3) pressures result in a loss of magnetic remanence
 249 in pyrrhotite (Figures 2A and B). Hydrostatic pressure demagnetization trends of absolute
 250 magnetic intensity overlap significantly below 1.24 GPa for samples with different domain-sizes
 251 (open grey symbols; measurements upon decompression are indicated by solid grey symbols).
 252 Complete demagnetization is achieved at ~ 2.8 GPa (Rochette et al., 2003). The demagnetization
 253 occurs upon compression and is mostly irreversible; only 3-6% of the initial remanent
 254 magnetization is recovered upon decompression from 1.24 GPa (Table 3; Bezaeva et al., 2007;
 255 submitted).

256 Demagnetization levels in shocked samples were determined using the total vector lengths of
 257 the alternating field demagnetization trends of the pre- and postshock remanences (Figure 3A).
 258 (Remaining magnetization fractions determined using absolute intensities yield results that differ
 259 by 2-4.3% in the SD/SP nodule, 0.4-7.8% in the MD single-crystal and 0-1% in the PSD schist,
 260 from those using the total vector length analysis.) Below ~ 3 GPa, the pure mineral results are
 261 remarkably consistent with the static demagnetization data (Figure 2A). However, at greater
 262 pressures (Figure 2B), shock does not result in complete demagnetization of pyrrhotite. In fact,
 263 the remaining remanence in the pure mineral phases increases with increasing pressure. This
 264 result cannot be attributed to the production of quenched metastable ferrimagnetic hexagonal
 265 pyrrhotite (Bennet and Graham, 1981) as heating was insufficient ($<210 - 230^\circ\text{C}$) to generate this

266 phase upon cooling. Also, it is not a result of the acquisition of shock remanent magnetization
267 because the impact velocities were much lower than those shown to produce impact generated
268 plasma magnetic fields (multiple km/s; Crawford and Schultz, 1988). One specimen initially
269 demagnetized prior to shock did not acquire a magnetic remanence at 3.30 GPa and postshock
270 remaining remanences do not possess a second component of magnetization related to the
271 direction of the ambient laboratory field (Figure 3).

272 The net increase in remanence in two outlying shocked specimens of the MD single-crystal
273 (Figure 2B) may be related to the orientation of the shock direction with respect to the basal
274 plane of pure pyrrhotite. Not all magnetic minerals are as anisotropic as pyrrhotite. Note that the
275 anisotropy of magnetic susceptibility in the PSD pyrrhotite-bearing schist (Table S4) is much
276 lower and, when shocked in two perpendicular directions, the schist results do not indicate
277 orientation dependence.

278 Alternating field demagnetization curves (Figure 4A) provide insight into changes in the
279 coercivity of pyrrhotite, and the slopes of the demagnetization curves (the coercivity spectra,
280 Figure 4B) provide information about the changes in the coercivity distribution in the sample.
281 Demagnetization curves of postshock remaining magnetization (solid line) are flat at low peak
282 field levels, indicating no magnetic remanence is removed at these levels during alternating field
283 demagnetization, as it has been preferentially removed as a result of pressure. In comparison, the
284 preshock saturation remanence curve (dashed line) has a negative slope. The coercivity fraction
285 demagnetized by (5.67 GPa) shock in the SD/SP nodule is located between 0 and 15 mT
286 (horizontal arrow in Figure 4B) consistent with previous pressure studies of magnetic minerals
287 (e.g., Cisowski and Fuller, 1978; Jackson et al., 1993).

288 The transition between the low pressure regime and the higher pressure regime
289 approximately coincides with the Hugoniot Elastic Limit of pyrrhotite at ~ 3.5 GPa. Several static
290 pressure studies observed a reversible magnetic transition to paramagnetism near this pressure
291 (Figure 2B). However, differences in the transition pressures are likely due to differences in
292 pressure calibration methods, equilibration time scales, non-hydrostatic contributions to stress,
293 and/or sample differences. The transition was observed at 4.5 ± 0.5 GPa (Kobayashi et al., 1997)
294 and between 1.2 and 3.8 GPa (LaBounty et al., submitted) in Mössbauer spectroscopy, and in
295 neutron diffraction experiments between 2.6 and 3.1 GPa (Rochette et al., 2003). X-ray
296 diffraction measurements under pressure indicate a change in lattice compressibility, but not a
297 discontinuous volume change, at 4.5 ± 0.5 GPa (Kobayashi et al., 1997) and at 6.2 GPa
298 (Kamimura et al., 1992). Lattice parameters of the postshock (recovered) SD/SP nodule (5.67
299 GPa) and MD single-crystal (6.92 GPa) are within error the same as their uncompressed
300 equivalents (Table S1). Earlier Mössbauer spectroscopy experiments placed the transition
301 between 0.5 and >1.6 GPa (Vaughan and Tossell, 1973). The onset of a phase change to a high
302 pressure phase was detected in shock experiments between 2.7 and 3.8 GPa (Ahrens, 1979, also
303 with uncertain pressures, T. Ahrens, personal communication).

304 The slope in demagnetization above 1.24 GPa is uncertain. Static pressure demagnetization
305 of one pyrrhotite sample (No. 98080, open grey squares in Figure 2) with the nonmagnetic
306 pressure cell capable of making magnetic measurements up to 1.8 GPa suggests that the
307 demagnetization slope is constant below 2 GPa. The slope of the demagnetization trend at
308 greater pressures and whether the static data approach the shock data is unknown at present.

309 *3.2 Permanent changes in the magnetic properties of shocked pyrrhotite*

310 Shock compression induces permanent changes in the intrinsic magnetic properties of
311 pyrrhotite. After shock, the material can acquire a greater remanence when strong fields are
312 applied, as illustrated by the isothermal remanent magnetization acquisition curve in Figure 5A.
313 Generally, samples shocked above a few GPa demonstrate an increase in saturation remanence
314 with pressure; however, there is significant scatter in the magnitude of the increase (Figure 5B).
315 Increase in saturation remanence is consistent with an increase in M_{rs}/M_s observed in the MD
316 single-crystal (Table S3; Louzada et al., 2007) and the PSD schist (Figure 6 in Gattacceca et al.,
317 2007b). The average M_{rs}/M_s ratios in the shocked SD/SP nodule are within 1σ error of the
318 unshocked nodule, with the exception of one specimen shocked at 2.81 GPa.

319 Changes in coercivity of pyrrhotite are indicated in Figures 4 and 6. Postshock resaturation
320 remanence spectra are broader than preshock spectra (compare the grey and dash-dotted lines in
321 Figures 4B and C), with their peaks displaced towards higher peak alternating field values. The
322 saturation remanent magnetization after shock is carried by fractions with a wider range of
323 coercivities, and the bulk of the magnetization is removed at greater fields than in the unshocked
324 case. All shocked specimens, except for one at low pressure (0.99 GPa), show an increase in the
325 median destructive field (the magnetic field required to remove half of the magnetization) and
326 the peak field of the coercivity spectra of saturation remanence after shock (compare open
327 symbols to closed symbols in Figures 6A and B). With increasing shock pressure, the magnitude
328 of both quantities increases.

329 In addition to the changes shown here, previous work has also shown an increase in the low
330 temperature memory of shocked pyrrhotite as it is cycled through the low temperature transition
331 at ~ 30 K (Figure S1; Louzada et al., 2007). The changes observed are consistent with stress (or
332 shock) hardening of the material. Increasing coercivity, saturation remanence, M_{rs}/M_s and low
333 temperature memory of pyrrhotite have been shown to correlate with decreasing grain and
334 domain-size (Dekkers, 1988, 1989; Dekkers et al., 1989). Increasing single-domain like behavior
335 of shocked and stressed materials has been observed in (titano-)magnetite bearing samples (e.g.,
336 Cisowski and Fuller, 1978; Gilder et al., 2004; Jackson et al., 1993) and may be a sensitive
337 indicator of shock in originally multidomain materials. Note that (within error) the change in
338 M_{rs}/M_s in the single-domain nodules is negligible (Table S3; Louzada et al., 2007).

339

340 4. Discussion

341 4.1 Stress effects on pyrrhotite

342 Hydrostatic experiments capable of measuring remanent magnetization while under pressure
343 show that demagnetization occurs upon the application of stress, rather than upon
344 decompression, and is mostly irreversible (Bezaeva et al., 2007; see also quasi-hydrostatic results
345 in Gilder et al., 2006). Recovery of remanence upon decompression is only a few percent in the
346 pyrrhotite samples investigated here. Although repeated stress cycling will reduce the
347 magnetization further, the bulk of the remanence loss occurs upon the first application of stress,
348 e.g., a second application of 1.24 GPa decreases the remaining remanence from 83% to 80% in
349 the MD single-crystal (open diamonds in Figure 2A).

350 In multidomain samples, magnetic domain reordering upon static compression, which is
351 irreversible upon decompression, may reduce magnetization (e.g., Borradaile and Jackson, 1993;
352 Nagata and Carleton, 1969). The fact that the intrinsic properties of hydrostatically stressed

353 samples do not change (e.g., saturation remanence and coercivity, Figures 5 and 6; Bezaeva et
354 al., 2007, submitted) indicates that the domain reordering is reversible upon resaturation (the
355 domain walls move to their original positions). This observation is consistent with the fact that
356 no permanent deformation or damage was observed upon visual inspection of statically stressed
357 pyrrhotite up to 3 GPa (Rochette et al., 2003).

358 In single-domain grains, pressure demagnetization cannot be attributed to domain wall
359 movements. Rather, changes in magnetostriction and magnetocrystalline anisotropy have been
360 invoked as a pressure demagnetization mechanism (e.g., Gilder et al., 2004; Kinoshita, 1968;
361 Nagata, 1966). Magnetocrystalline anisotropy is a result of crystallographic symmetry of
362 ferromagnetic minerals. Magnetostriction is the spontaneous change in shape of a crystal lattice
363 when magnetized and a consequence of the strain dependence of magnetocrystalline anisotropy
364 (e.g., Dunlop and Özdemir, 1997, p. 42). An external magnetic field will result in a change in
365 exchange interactions between ions, which in turn results in a change in the interionic distances,
366 increasing in some directions and decreasing in others depending on the magnetic anisotropy.
367 Conversely, external stress can cause a change in shape of the crystal lattice, resulting in
368 increased or diminished interactions between adjacent ions, and a change in the magnetization.
369 Materials with a positive magnetostriction expand in the direction of a magnetic field and
370 contract in the transverse directions. If the lattice is constrained however, e.g., due to an external
371 stress, then magnetostriction will not be accommodated and magnetostrictive strain energy arises
372 (Nagata and Kinoshita, 1967). The field required to overcome this magnetostrictive energy
373 increases with external stress. In the absence of a field, the spontaneous magnetization in the
374 crystal will rotate away from the stress axis. If there were no internal stresses in crystals, then we
375 would expect the stress effects on remanence to be reversible upon decompression and equal
376 with each application of stress. However, observations of irreversibility and decreasing
377 efficiency of demagnetization with the number of stress cycles imply that threshold energies for
378 domain restructuring are locally overcome (e.g., Kinoshita, 1968).

379 4.2 Grain damage

380 The two specimens that were subjected to hydrostatic compression up to 1.24 or 1.8 GPa do
381 not show any permanent changes in their magnetic properties, probably because the pressures
382 were too low to cause irreversible deformation or damage to the pyrrhotite. Pyrrhotite recovered
383 upon decompression from 3 GPa in quasi-hydrostatic experiments did not show any signs of
384 significant shape change or loss of coherence upon visual inspection either (Rochette et al.,
385 2003). In contrast, pervasive fracturing was observed in microscope images of the nodule, single-
386 crystal, and schist specimens shocked to pressures over 2.81 GPa (Figure S6). Fracturing can be
387 more intense around the outer perimeter of the disc-shaped specimen, radial, or make 60° angles.

388 Microfracturing has been invoked in experimentally shocked (explosive) magnetite-bearing
389 rocks as a cause of hysteresis modification (Gattacceca et al., 2007b). Fracturing and/or
390 dislocation/defect generation impeding motion of domain walls has also been invoked in
391 hydrostatic stress experiments up to 6 GPa (Gilder et al., 2004; Gilder and Le Goff, 2008). If
392 dilatational fractures subdivide large grains into smaller multidomain or single-domain grains,
393 then fracturing may lead to the observed magnetic hardening. An evaluation of the types of
394 magnetic interactions between the domains in the pyrrhotite before and after shock (Figure S7)
395 indicates that the nodule consists of nearly purely noninteracting single-domains, and the
396 changes in interactions in the MD pyrrhotite are consistent with a decrease in grain size (a
397 decrease in the net demagnetizing effect).

398 4.3 *Magnetic domain imaging*

399 In Bitter (1931) imaging, magnetic colloid is attracted to domain and grain boundaries
400 making them appear dark in the image, whereas homogeneously magnetized or nonmagnetic
401 regions appear bright. The magnetic monoclinic pyrrhotite in the single-crystal is organized into
402 long, thin stripes (30-55 μm wide and up to >1 mm long) at $\sim 60^\circ$ to one another, intergrown with
403 antiferromagnetic (nonmagnetic) hexagonal pyrrhotite (Figure 7A) (Pósfai et al., 2000; Soffel,
404 1981). Assuming that these magnetic stripes continue in the c -plane (perpendicular to the page),
405 the stripes are interpreted as lamellae (sub-) parallel to the $(00l)$ plane (Kontny et al., 2000, and
406 references therein). Detailed magnetic force microscopy images of the magnetic lamellae (Figure
407 7B) reveal a set of simply arranged parallel dark and bright lines, with a spatial scale of ~ 1 μm
408 by 12 to 33 μm (but possibly longer), corresponding to regions where magnetic flux is going into
409 or coming out of the plane, respectively, and are interpreted as magnetic domains (e.g., Bennet et
410 al., 1972) separated by 180° domain walls (in the walls the magnetization rotates 180°). Other
411 observations of average domain width in pyrrhotite are variable: ~ 4 -8 μm (Halgedahl and Ye,
412 2000) and 100-200 nm (Pósfai et al., 2000). Pósfai et al. (2000) observed (large scale) lamellae
413 widths of ~ 30 μm , similar to the lamellae reported above. Bitter and magnetic force microscopy
414 images of the surface parallel to $(00l)$ (the basal plane) of the unshocked MD single-crystal show
415 broad regions of grey, indicating magnetization is mostly confined to the plane (Figures 7C and
416 D), consistent with pyrrhotite having a strong crystalline magnetic anisotropy. The unshocked
417 SD/SP nodule has smaller lamellae, which also make $\sim 60^\circ$ angles with one another (Figure S8).

418 Bitter images of postshock specimens (Figures 7E and I) reveal pervasive fracturing.
419 Magnetic force imaging indicates that the magnetic domains are still sub-parallel to $(00l)$, but
420 that the boundaries between the domains undulate (Figures 7F and J). Sinuous lines (white
421 arrows in Figure 7F) cross-cut the lamellae, and although the widths of the lamellae have not
422 changed (<1 to 2 μm), the lengths of the domains appear to be shorter. The perpendicular view
423 $(00l)$ shows broad swaths of chaotic bright and dark regions (Figures 7H and L). Due to the
424 isolated distribution of smaller domains in the nodule, it is hard to draw conclusions from the
425 postshock recovered pyrrhotite images (Figure S8).

426 Due to the strong crystalline anisotropy, the domain patterns of pyrrhotite are insensitive to
427 thinning or stresses induced by polishing (Halgedahl and Ye, 2000). Progressively higher peak
428 alternating field demagnetization normally results in more planar 180° domain walls and a
429 simpler domain distribution in pyrrhotite (Halgedahl and Fuller, 1981). The fact that the domains
430 in AF demagnetized (~ 85 mT) shocked pyrrhotite are undulated, suggests that the domain walls
431 are pinned and cannot move to a more energetically favorable parallel arrangement under
432 alternating fields. Soffel (1981) found that curved domain walls occur only in regions of high
433 inclusion or dislocation density. Planar defect structures, kink-bands and bended twin lamellae in
434 pyrrhotite in a polymict impact breccia from Bosumtwi crater (Kontny et al., 2007) were also
435 attributed to brittle and/or brittle-ductile deformation features and nanoscale fracturing resulting
436 from differential stresses associated with the shock wave. Such shock-induced substructures have
437 been invoked to explain the magnetic hardness of pyrrhotite in the Martian shergottite meteorites
438 as well (Rochette et al., 2001).

439 4.4 *Generalization of the results*

440 The pressure demagnetization seen in this study generally holds for all other magnetic phases
441 previously studied. Low coercivity magnetization is preferentially demagnetized in all minerals

442 (Bezaeva et al., 2007, submitted; Cisowski and Fuller, 1978; Gattacceca et al., 2007b; Louzada et
443 al., 2007) upon compression (Bezaeva et al., 2007; Nagata and Kinoshita, 1964; Nagata, 1966).
444 Repeated low pressure shock experiments of igneous rocks also indicate that the first application
445 of stress results in the greatest loss of initial remanence (Nagata, 1971; Pohl et al., 1975).
446 Magnetic hardening (Gilder et al., 2004; Jackson et al., 1993; Kontny et al., 2007) has been
447 proposed as a potential magnetic indicator of low (a few GPa) pressure shock in multidomain
448 fractions in naturally shocked basalts (Cisowski and Fuller, 1978; Louzada et al., 2008). The use
449 of shocked magnetic minerals as indicators of paleofield intensity is complicated by the fact that
450 both magnetic remanence and magnetic properties are affected by shock.

451 A compilation of demagnetization experiment results suggests that pressure demagnetization
452 levels of different minerals (titanomagnetite, titanohematite and pyrrhotite) are not unique at low
453 pressures (Louzada et al., in preparation) and therefore not predictable a priori. However, within
454 each group, the demagnetization at 1.24 GPa is a function of coercivity and roughly proportional
455 to $\ln(B_{cr})$ (Bezaeva et al., submitted). Different demagnetization mechanisms may be active in
456 different minerals and, within a single mineralogy, demagnetization may be composition, domain
457 state and/or phase dependant.

458 *4.5 Implications for the Martian crust*

459 The stability of pyrrhotite in the Martian crust is controlled by the lithostatic pressure and
460 geothermal gradient. At the base of the crust, ~50-100 km depth (Zuber, 2001), the lithostatic
461 pressure on Mars is only ~0.5-1 GPa. We assume that lithostatic pressure demagnetization of the
462 Martian crust is negligible. Although the pressure dependence of the Curie temperature of
463 pyrrhotite (320°C) is unknown, we assume that it is negligible as well. Based on thermal
464 evolution models, remanence in pyrrhotite was stable at depths up to ~50 km (Arkani-Hamed,
465 2005) in the ancient crust of Mars.

466 Since the formation of the Martian crust, the vertical extent of the magnetized layer has likely
467 been reduced. Thermoviscous decay of remanence at depth in the absence of a global field may
468 have raised the lower boundary of the magnetized crust (Shahnas and Arkani-Hamed, 2007).
469 Based on cratering statistics, numerous impacts over Mars' history may have generated shock
470 pressures of a few GPa capable of partially demagnetizing the upper ~10-20 km globally
471 (Arkani-Hamed, 2005). Secondary impacts from large basin forming events are also capable of
472 demagnetizing the upper crust around basins greater than ~500 km in diameter (Artemieva et al.,
473 2005). However, since the initial shock event should result in the greatest reduction of
474 magnetization, the demagnetization effects of multiple impacts over time can be disregarded in
475 this discussion.

476 In the pressure range suggested to be responsible for shock demagnetization of the Martian
477 crust around Hellas basin (Louzada and Stewart, in press), the observed reduction of
478 magnetization of saturation remanence in pyrrhotite indeed makes pyrrhotite a candidate for
479 Mars. The presence of pyrrhotite in the Martian crust would have interesting implications for the
480 chemistry of Mars. Pyrrhotite is an important magnetic carrier in magmatic and metamorphic
481 terrains on Earth. On Mars, it is likely a primary igneous mineral if the crust and mantle are
482 indeed relatively enriched in Fe and S (Longhi et al., 1992). To date, pyrrhotite has not been
483 observed, or inferred from, in situ rover experiments on Mars or from spacecraft observations;
484 pyrrhotite at the surface may not be preserved due to oxidation and weathering.

485 The simultaneous shock demagnetization of the PSD schist in two perpendicular directions

486 yields similar demagnetization values (Figure 2B), as opposed to the pure MD single-crystal,
487 which exhibits strong orientation-dependent demagnetization. With its lower magnetic
488 anisotropy ($P = 1.741$, $T = 0.697$), the PSD schist is certainly a much better analogue than our
489 pure pyrrhotite samples of the Martian shergottites ($P = 1.059 \pm 0.027$, $T = 0.21$) (Gattacceca et
490 al., 2008) and the Martian crust. We suggest that magnetic anisotropy effects can generally be
491 ignored in the interpretation of shock demagnetization of the Martian crust.

492 However, a number of outstanding questions remain regarding the nature of the Martian
493 magnetic crust. The magnetic mineral distribution on Mars has to satisfy both the high intensity
494 and pressure demagnetization of the crust. Even accounting for the increase in saturation
495 remanence as a result of shock on magnetic minerals, the localized high intensity of the Martian
496 magnetization has not been satisfactorily explained at present. Although a strong (10 times Earth,
497 or several hundred microtesla) paleofield could in principle account for this, recent
498 paleointensity analyses of the 4 Ga Martian field from the meteorite ALH84001 suggest the field
499 was only of order 50 microtesla (Weiss et al., 2008). Since pressure demagnetization
500 preferentially removes the low coercivity fraction of the magnetization (Figures 4B and C), and
501 isothermal remanent magnetization has a lower coercivity than thermoremanent magnetization,
502 pressure demagnetization of the Martian basaltic crust may be less efficient and has not been
503 adequately quantified at present. Finally, the interpretation of the distribution of the
504 magnetization in the crust is dependent on the poorly constrained coherence scale of the
505 magnetization, resolution limitations of the magnetic field maps, the possible spatial distribution
506 of magnetic minerals and intensity.

507

508 **5. Conclusions**

509 Impact demagnetization of the Martian crust has been inferred from the distribution of crustal
510 magnetic fields in relation to the youngest impact basins. Estimates of the shock pressures
511 required to demagnetize crustal materials are on the order of a few GPa. In this study, we
512 examine the effect of static and dynamic compression on the magnetic remanence and intrinsic
513 magnetic properties of natural pyrrhotite, a potential carrier of the magnetization in the Martian
514 crust, of varying magnetic domain-size up to 12 GPa.

515 Both static and dynamic compression of pyrrhotite result in a preferential demagnetization of
516 the low coercivity components. The pressure demagnetization results can be divided into two
517 regimes approximately separated by the ferri- to paramagnetic transition in pyrrhotite at 3-4.5
518 GPa. This transition also coincides with the Hugoniot Elastic Limit (~ 3.5 GPa), the onset of a
519 broad transition region along the Hugoniot to a high-pressure phase, and a change in the lattice
520 compressibility of pyrrhotite. We cannot say at present whether the phenomena are related. It is
521 possible that the Hugoniot Elastic Limit coincides with the structural phase transition, or that
522 there is a small pressure range in which the pressure wave remains in the initial phase. This
523 question cannot be resolved with the data at present and more shock experiments to determine
524 the Hugoniot equation of state of pyrrhotite are needed.

525 Hydrostatic pressures below the Hugoniot Elastic Limit, do not show permanent changes in
526 the magnetic properties, probably because the pressures were too low to cause damage to the
527 crystal structure. Permanent changes do occur for pyrrhotite shocked to greater pressures and
528 include an increase in saturation remanence and an increase in the bulk coercivity of the material.
529 These observations are attributed to microfracturing and pinning of domain walls, resulting in

530 more single-domain like behavior and magnetic hardening. Bitter imaging and magnetic force
531 microscopy of the shocked samples reveals undulating and sinuous domain boundaries compared
532 to unshocked pyrrhotite with simple, linear 180° domain walls.

533 The changes in magnetic remanence and magnetic properties generally hold for all magnetic
534 minerals. However, there are differences between the experimental results on pure pyrrhotite
535 minerals and pyrrhotite-bearing rocks. The direction of shock with respect to magnetic
536 anisotropy or rock fabric does not appear to be an important factor in the magnitude of
537 demagnetization in pyrrhotite-bearing schists. We conclude that pyrrhotite remains a potential
538 carrier of the magnetization in the Martian crust where it has likely been partially demagnetized
539 by shock.

540

541 **Acknowledgements**

542 Thanks to G. Kennedy (Kumamoto U.), L. Farina, W. Croft, C. Francis, R. Staples, D.
543 Lange, F. Ilievski, P. Hedman (Harvard), M. Jackson, J. Bowles, P. Sølheid, B. Moskowicz, J.
544 Feinburg (IRM, U. of Minnesota), J. Kirschvink, I. Hilburn, T. Raub (Caltech), D. Evans, R.
545 Mitchell, I. Rose, Taylor Kilian (Yale), R. Kopp (Princeton), P. Rochette (CEREGE), S. Bogue
546 (Occidental Coll.), C. Ross, V. Sivakumar (MIT). K.L.L. was supported by the Amelia Earhart
547 Fellowship (Zonta Int.), and the IRM Visiting Researcher Fellowship. This research is supported
548 by NASA Mars Fundamental Research Program (NNG04GD17G and NNX07AQ69G).

549

550 **References**

- 551 Acuña, M.H., J.E.P. Connerney, N.F. Ness, R.P. Lin, D. Mitchell, C.W. Carlson, J. McFadden,
552 K.A. Anderson, H. Rème, C. Mazelle, D. Vignes, P. Wasilewski and P. Cloutier, 1999.
553 Global Distribution of Crustal Magnetization Discovered by the Mars Global Surveyor
554 MAG/ER Experiment. *Science* 284, 790-793, doi:10.1126/science.284.5415.790.
- 555 Ahrens, T.J., 1979. Equations of State of Iron Sulfide and Constraints on the Sulfur Content of
556 the Earth. *JGR* 84, 985-998.
- 557 Antretter, M. and M. Fuller, 2002. Paleomagnetism and rock magnetism of martian meteorite
558 ALH 84001. *Physics and Chemistry of the Earth* 27, 1299-1303, doi:10.1016/S1474-
559 7065(02)00134-1.
- 560 Arkani-Hamed, J., 2005. Magnetic crust of Mars. *JGR* 110, doi:10.1029/2004JE002397.
- 561 Artemieva, N., L. Hood and B.A. Ivanov, 2005. Impact demagnetization of the Martian crust:
562 Primaries versus secondaries. *GRL* 32, doi:10.1029/2005GL024385.
- 563 Bennet, G.E.G., J. Graham and M.R. Thornber, 1972. New observations on natural pyrrhotites -
564 Part I. Mineragraphic Techniques. *American Mineralogist* 57, 445-462.
- 565 Bennet, G.E.G. and J. Graham, 1981. New observations on natural pyrrhotite: magnetic
566 transition in hexagonal pyrrhotite. *American Mineralogist* 66, 1254-1257.
- 567 Bertaut, E.F., 1953. Contribution à l'étude des structures lacunaires: La pyrrhotine. *Acta*
568 *Crystallographica* 6, 557-561, doi:10.1107/S0365110X53001502.

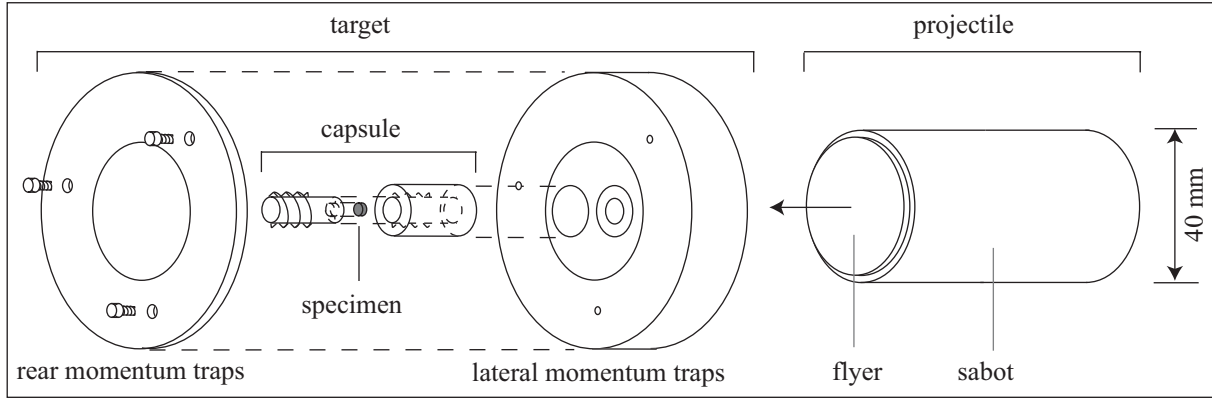
- 569 Bezaeva, N.S., P. Rochette, J. Gattacceca, R.A. Sadykov and V.I. Trukhin, 2007. Pressure
570 demagnetization of the Martian crust: Ground truth from SNC meteorites. *GRL* 34, L23202,
571 doi:10.1029/2007GL031501.
- 572 Bezaeva, N.S., J. Gattacceca, P. Rochette, R.A. Sadykov and V.I. Trukhin, submitted. An
573 overview of the demagnetization of terrestrial and extraterrestrial rocks under hydrostatic
574 pressure up to 1.2 GPa. *PEPI*.
- 575 Bitter, F., 1931. On Inhomogeneities in the Magnetization of Ferromagnetic Materials. *Phys.*
576 *Rev.* 38, 1903-1905, doi:10.1103/PhysRev.38.1903.
- 577 Borradaile, G.J. and M. Jackson, 1993. Changes in magnetic remanence during simulated deep
578 sedimentary burial. *PEPI* 77, 315-327.
- 579 Cisowski, S.M. and M. Fuller, 1978. The Effect of Shock on the Magnetism of Terrestrial Rocks.
580 *JGR* 83, 3441-3458.
- 581 Collinson, D.W., 1986. Magnetic properties of Antarctic shergottite meteorites EETA 79001 and
582 ALHA 77005: possible relevance to a Martian magnetic field. *EPSL* 77 (2), 159-164,
583 doi:10.1016/0012-821X(86)90157-3.
- 584 Crawford, D.A. and P.H. Schultz, 1988. Laboratory observations of impact-generated magnetic
585 fields. *Nature* 336, 50-52.
- 586 Dekkers, M.J., 1988. Magnetic properties of natural pyrrhotite Part I: Behaviour of initial
587 susceptibility and saturation-magnetization-related rock-magnetic parameters in a grain-size
588 dependent framework. *PEPI* 52, 376-393.
- 589 Dekkers, M.J., 1989. Magnetic properties of natural pyrrhotite. II High- and low-temperature
590 behaviour of Jrs and TRM as function of grain size. *PEPI* 57, 266-283.
- 591 Dekkers, M.J., J.L. Mattei, G. Fillion and P. Rochette, 1989. Grain-Size Dependence of the
592 Magnetic-Behavior of Pyrrhotite During Its Low-Temperature Transition at 34-K. *GRL* 16,
593 855-858.
- 594 Dunlop, D.J. and Ö. Özdemir, 1997. *Rock Magnetism - Fundamentals and Frontiers*, Cambridge
595 University Press, Cambridge.
- 596 Fleet, M.E., 1968. On the lattice parameters and superstructures of pyrrhotites. *The American*
597 *Mineralogist* 53, 1846-1855.
- 598 Frey, H., 2008. Ages of very large impact basins on Mars: Implications for the late heavy
599 bombardment in the inner solar system. *GRL* 35, L13203, doi:10.1029/2008GL033515.
- 600 Gattacceca, J. and P. Rochette, 2004. Toward a robust normalized magnetic paleointensity
601 method applied to meteorites. *EPSL* 227, 377-393.
- 602 Gattacceca, J., L. Berthe, M. Boustie, F. Vadeboin, P. Rochette and T. De Resseguier, 2007a. On
603 the efficiency of shock remanent processes. *PEPI*, doi:10.1016/j.pepi.2007.1009.1005.
- 604 Gattacceca, J., A. Lamali, P. Rochette, M. Boustie and L. Berthe, 2007b. The effects of
605 explosive-driven shocks on the natural remanent magnetization and the magnetic properties
606 of rocks. *PEPI* 162, 85-98, doi:10.1016/j.pepi.2007.1003.1006.

- 607 Gattacceca, J., P. Rochette, M. Gounelle and M. Van Ginneken, 2008. Magnetic anisotropy of
608 HED and Martian meteorites and implications for the crust of Vesta and Mars. *EPSL* 270 (3-
609 4), 280-289, doi:10.1016/j.epsl.2008.03.047.
- 610 Gilder, S.A., M. LeGoff, J.-C. Chervin and J. Peyronneau, 2004. Magnetic properties of single
611 and multi-domain magnetite under pressures from 0 to 6 GPa. *GRL* 31 (10),
612 doi:10.1029/2004GL019844.
- 613 Gilder, S.A., M. Le Goff and J.-C. Chervin, 2006. Static stress demagnetization of single and
614 multi-domain magnetite with implications for meteorite impacts. *High Pressure Research* 26
615 (4), 539-547, doi:10.1080/08957950601092085.
- 616 Gilder, S.A. and M. Le Goff, 2008. Systematic pressure enhancement of titanomagnetite
617 magnetization. *GRL* 35, L10302, doi:10.1029/2008GL033325.
- 618 Halgedahl, S. and J. Ye, 2000. Observed effects of mechanical grain-size reduction on the
619 domain structure of pyrrhotite. *EPSL* 176, 457-467.
- 620 Halgedahl, S.L. and M. Fuller, 1981. The dependence of magnetic domain structure upon
621 magnetization state in polycrystalline pyrrhotite. *PEPI* 26, 93-97.
- 622 Hood, L.L., N.C. Richmond, E. Pierazzo and P. Rochette, 2003. Distribution of crustal magnetic
623 fields on Mars: Shock effects of basin-forming impacts. *GRL* 30, 1281-1284,
624 doi:10.1029/2002GL016657.
- 625 Hrouda, F., 2007. Anisotropy of magnetic susceptibility of rocks in the Rayleigh Law region:
626 modelling errors arising from linear fit to non-linear data. *Studia Geophysica & Geodaetica*
627 51, 423-438, doi:10.1007/s11200-007-0024-5.
- 628 Jackson, M., G. Borradaile, P. Hudleston and S. Banerjee, 1993. Experimental Deformation of
629 Synthetic Magnetite-Bearing Calcite Sandstones: Effects on Remanence, Bulk Magnetic
630 Properties, and Magnetic Anisotropy. *JGR* 98 (B1), 383-401.
- 631 Jelínek, V., 1973. Precision A.C. bridge set for measuring magnetic susceptibility of rocks and
632 its anisotropy. *Studia Geophysica & Geodaetica* 17, 36-48, doi:10.1007/BF01614027.
- 633 Kamimura, T., M. Sato, H. Takahasi, N. Mori, H. Yoshida and T. Kaneko, 1992. Pressure-
634 induced phase transition in Fe-Se and Fe-S systems with a NiAs-type structure. *Journal of*
635 *Magnetism and Magnetic Minerals* 104-107, 255-256, doi:10.1016/0304-8853(92)90787-O.
- 636 Kinoshita, H., 1968. Studies on Piezo-Magnetization (III)-PRM and Relating Phenomena-. *J.*
637 *Geomagn. Geoelectr.* 20 (3), 155-167.
- 638 Kirichenko, A.S., A.V. Kornilov and V.M. Pudalov, 2005. Properties of Polyethylsiloxane as a
639 Pressure-Transmitting Medium. *Instruments and Experimental Techniques* 48 (6), 813-816,
640 doi:10.1007/s10786-005-0144-5.
- 641 Kletetschka, G., J.E.P. Connerney, N.F. Ness and M.H. Acuña, 2004. Pressure effects on martian
642 crustal magnetization near large impact basins. *MAPS* 39, 1839-1848.
- 643 Kobayashi, H., M. Sato, T. Kamimura, M. Sakai, H. Onodera, N. Kuroda and Y. Yamaguchi,
644 1997. The effect of pressure on the electronic states of FeS and Fe₇S₈ studied by Mössbauer
645 spectroscopy. *Journal of Physics: Condensed Matter* 9, 515-527, doi: 10.1088/0953-
646 8984/9/2/019.

- 647 Kontny, A., H. de Wall, T.G. Sharp and M. Pósfai, 2000. Mineralogy and magnetic behavior of
648 pyrrhotite from a 260 C section at the KTB drilling site, Germany. *American Mineralogist*
649 85, 1416-1427.
- 650 Kontny, A., T. Elbra, J. Just, L.J. Pesonen, A.M. Schleicher and J. Zolk, 2007. Petrography and
651 shock-related remagnetization of pyrrhotite in drill cores from the Bosumtwi Impact Crater
652 Drilling Project, Ghana. *MAPS* 42 (4/5), 811-827.
- 653 LaBounty, D., J. Hustoft, S.-H. Shim, J. Zhao and W. Sturhahn, submitted. Synchrotron
654 Mössbauer Spectroscopy of Pyrrhotite up to 6.9 GPa and Implications for Planetary
655 Magnetic Record. *Journal of Synchrotron Radiation*.
- 656 Langel, R.A., J.D. Phillips and R.J. Horner, 1982. Initial scalar magnetic anomaly map from
657 MAGSAT. *GRL* 9 (4), 269-272.
- 658 Lillis, R.J., D.L. Mitchell, R.P. Lin, J.E.P. Connerney and M.H. Acuña, 2004. Mapping crustal
659 magnetic fields at Mars using electron reflectometry. *GRL* 31, doi:10.1029/2004GL020189.
- 660 Lillis, R.J., H.V. Frey and M. Manga, 2008a. Rapid decrease in Martian crustal magnetization in
661 the Noachian era: Implications for the dynamo and climate of early Mars. *GRL* 35, L14203,
662 doi:10.1029/2008GL034338.
- 663 Lillis, R.J., H.V. Frey, M. Manga, D.L. Mitchell, R.P. Lin, M.H. Acuña and S.W. Bougher,
664 2008b. An improved crustal magnetic field map of Mars from electron reflectometry:
665 Highland volcano magmatic history and the end of the martian dynamo. *Icarus* 194, 575-596,
666 doi:10.1016/j.icarus.2007.09.032.
- 667 Longhi, J., E. Knittle, J.R. Holloway and H. Wänke, 1992. 6. The bulk composition, mineralogy
668 and internal structure of Mars, in: Kieffer, H.H., B.M. Jakosky, C.W. Snyder and M.S.
669 Matthews (Eds), *Mars*. The University of Arizona Press, Tuscon, pp. 184-208.
- 670 Louzada, K.L., S.T. Stewart and B.P. Weiss, 2007. Effect of shock on the magnetic properties of
671 pyrrhotite, the Martian crust, and meteorites. *GRL* 34, L05204, doi:10.1029/2006GL027685.
- 672 Louzada, K.L., B.P. Weiss, A.C. Maloof, S.T. Stewart, N.L. Swanson-Hysell and S.A. Soule,
673 2008. Paleomagnetism of Lonar impact crater, India. *EPSL* 275 (3-4), 308-319,
674 doi:10.1016/j.epsl.2008.08.025.
- 675 Louzada, K.L. and S.T. Stewart, in press. Effects of Planet Curvature and Crust on the Shock
676 Pressure Field around Impact Basins. *GRL*, doi:10.1029/2009GL03786.
- 677 Martín-Hernández, F., M.J. Dekkers, I.M.A. Bominaar-Silkens and J.C. Maan, 2008. Magnetic
678 anisotropy behaviour of pyrrhotite as determined by low- and high-field experiments. *GJI*
679 174, 42-54, doi: 10.1111/j.1365-246X.2008.03793.x.
- 680 McGlaun, J.M., S.L. Thompson and M.G. Elrick, 1990. CTH: A 3-dimensional shock-wave
681 physics code. *Int. J. Impact Eng.* 10, 351-360, doi:10.1016/0734-743X(90)90071-3.
- 682 McSween Jr, H.Y. and A.H. Treiman, 1998. Chapter 6: Martian meteorites, in: Papike, J.J. (Eds),
683 *Planetary Materials*. pp. 53.
- 684 Melosh, H.J., 1989. *Impact Cratering: A Geologic Process*, Oxford University Press, New York.
- 685 Menyeh, A. and W. O'Reilly, 1991. The magnetization process in monoclinic pyrrhotite (Fe₇S₈)
686 particles containing few domains. *GJI* 104 (2), 387-399.

- 687 Mohit, P.S. and J. Arkani-Hamed, 2004. Impact demagnetization of the martian crust. *Icarus*
688 168, 305-317, doi:10.1016/j.icarus.2003.12.005.
- 689 Morimoto, N., A. Gyobu, K. Tsukuma and K. Koto, 1975. Superstructure and nonstoichiometry
690 of intermediate pyrrhotite. *American Mineralogist* 60 (3-4), 240-248.
- 691 Nagata, T. and H. Kinoshita, 1964. Effect of Release of Compression on Magnetization of Rocks
692 and Assemblies of Magnetic Minerals. *Nature* 204, 1183-1184.
- 693 Nagata, T., 1966. Main Characteristics of Piezo-Magnetization and Their Qualitative
694 Interpretation. *J. Geomagn. Geoelectr.* 18 (1), 81-97.
- 695 Nagata, T. and H. Kinoshita, 1967. Effect of hydrostatic pressure on magnetostriction and
696 magnetocrystalline anisotropy of magnetite. *PEPI* 1, 44-48.
- 697 Nagata, T. and B.J. Carleton, 1969. Notes on Piezo-remnant Magnetization of Igneous Rocks II.
698 *J. Geomagn. Geoelectr.* 21 (1), 427-445.
- 699 Nagata, T., 1971. Introductory Notes on Shock Remnant Magnetization and Shock
700 Demagnetization of Igneous Rocks. *Pure and Appl. Geophys.* 89, 159-177.
- 701 Nkoma, J.S. and G. Ekosse, 1999. X-ray diffraction of chalcopyrite CuFeS_2 , pentlandite
702 $(\text{Fe,Ni})_9\text{S}_8$ and pyrrhotite Fe_{1-x}S obtained from Cu-Ni ore bodies. *Journal of Physics:*
703 *Condensed Matter* 11, 121-128.
- 704 Pohl, J., U. Bleil and U. Hornemann, 1975. Shock Magnetization and Demagnetization of Basalt
705 by Transient Stress up to 10 kbar. *Journal of Geophysics* 41, 23-41.
- 706 Pósfai, M., T.G. Sharp and A. Kontny, 2000. Pyrrhotite varieties from the 9.1 km deep borehole
707 of the KTB project. *American Mineralogist* 85, 1406-1415.
- 708 Rochette, P., J.-L. Mattéi and M.J. Dekkers, 1990. Magnetic transition at 30-34 Kelvin in
709 pyrrhotite: insight into a widespread occurrence of this mineral in rocks. *EPSL* 98, 319-328.
- 710 Rochette, P., J.-P. Lorand, G. Fillion and V. Sautter, 2001. Pyrrhotite and the remanent
711 magnetization of SNC meteorites: a changing perspective of Martian magnetism. *EPSL* 190,
712 1-12.
- 713 Rochette, P., G. Fillion, R. Ballou, F. Brunet, B. Ouladdiaf and L. Hood, 2003. High pressure
714 magnetic transition in pyrrhotite and impact demagnetization on Mars. *GRL* 30,
715 doi:10.1029/2003GL017359.
- 716 Rochette, P., J. Gattacceca, V. Chevrier, V. Hoffmann, J.-P. Lorand, M. Funaki and R.
717 Hochleitner, 2005. Matching Martian crustal magnetization and magnetic properties of
718 Martian meteorites. *MAPS* 40, 529-540.
- 719 Sadykov, R.A., N.S. Bezaeva, A.I. Kharkovskiy, P. Rochette, J. Gattacceca and V.I. Trukhin,
720 2008. Nonmagnetic high pressure cell for magnetic remanence measurements up to 1.5 GPa
721 in a superconducting quantum interference device magnetometer. *Review of Scientific*
722 *Instruments* 79 (11), 115102, doi:10.1063/1.2999578.
- 723 Sekine, T., T. Kobayashi, M. Nishio and E. Takahashi, 2008. Shock equation of state of basalt.
724 *Earth Planets and Space* 60 (9), 999-1003.
- 725 Shahnas, H. and J. Arkani-Hamed, 2007. Viscous and impact demagnetization of Martian crust.
726 *JGR* 112 (E02009), doi:10.1029/2005JE002424.

- 727 Soffel, H., 1977. Pseudo-single-domain effects and single domain-multidomain transition in
728 natural pyrrhotite deduced from domain-structure observations. *Journal of Geophysics* 42 (4),
729 351-359.
- 730 Soffel, H.C., 1981. Domain structure of natural fine-grained pyrrhotite in a rock matrix
731 (diabase). *PEPI* 26, 98-106, doi:10.1016/0031-9201(81)90102-3.
- 732 Stewart, S.T., The shock compression laboratory at Harvard: A new facility for planetary impact
733 processes, *Lunar and Planetary Science XXXV*, Lunar and Planetary Institute, Houston, TX,
734 2004, p. Abs. No. 1290.
- 735 Vaughan, D.J. and J.A. Tossell, 1973. Magnetic Transitions Observed in Sulfide Minerals at
736 Elevated Pressures and Their Geophysical Significance. *Science* 179, 375-377,
737 doi:10.1126/science.179.4071.375.
- 738 Weiss, B.P., H. Vali, F.J. Baudenbacher, J.L. Kirschvink, S.T. Stewart and D.L. Shuster, 2002.
739 Records of an ancient Martian magnetic field in ALH84001. *EPSL* 201, 449-463.
- 740 Weiss, B.P., L.E. Fong, H. Vali, E.A. Lima and F.J. Baudenbacher, 2008. Paleointensity of the
741 ancient Martian magnetic field. *GRL* 35, L23207, doi:10.1029/2008GL035585.
- 742 Yund, R.A. and H.T. Hall, 1969. Hexagonal and Monoclinic Pyrrhotites. *Economic Geology* 64,
743 420-423.
- 744 Zuber, M.T., 2001. The crust and mantle of Mars. *Nature* 412, 220-227, doi:10.1038/35084163.
745
746
747



748

749

750

751

752

753

754

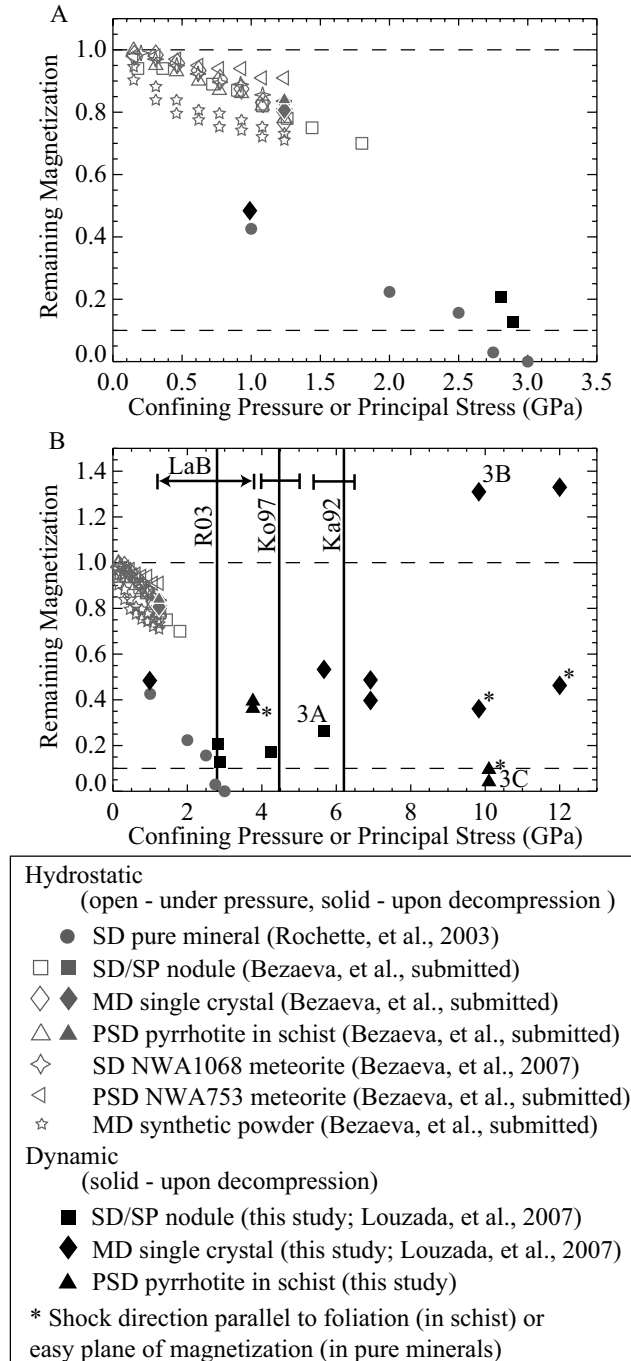
755

756

757

758

Figure 1 Example schematic diagram of an aluminum target configuration for a shock recovery experiment. Other configurations have a single capsule placed off-center. The inner capsule is smaller than the inner diameter of the 2G magnetometer. The disc-shaped specimens (3-12 mm diameter \times <1 mm thick) are positioned approximately 1.5 mm from the impact surface. Self-shorting gauges attached to the impact side of the target assembly record the tilt of the projectile (generally <10 mrad). Redundant impact velocity measurements are performed by shorting pins and lasers placed in the path of the projectile prior to impact. The impact occurs in vacuum (<100 mTorr) at room temperature in the ambient magnetic field. The target assembly is decelerated and recovered downrange in a rag-filled catch tank.



759

760

761

762

763

764

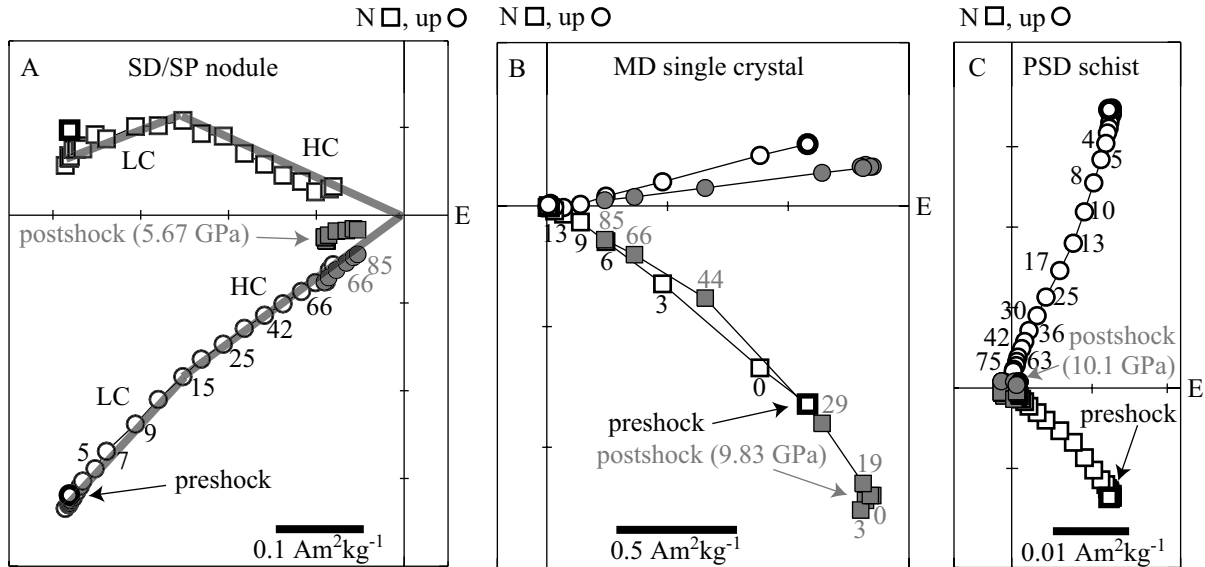
765

766

767

768

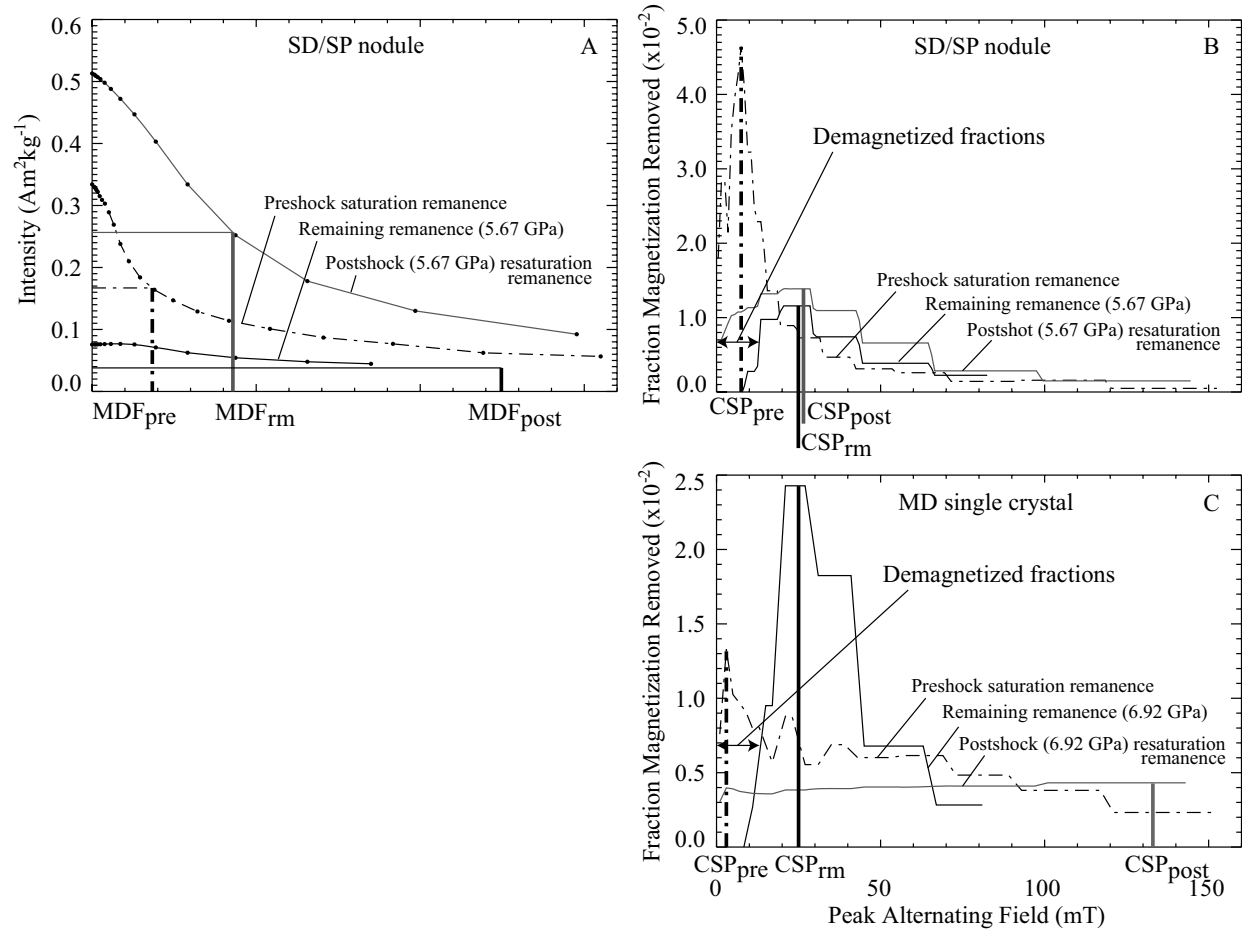
Figure 2 Demagnetization results of hydrostatic and dynamic experiments on pyrrhotite. Panel (A) is a detail of (B). Shocked samples are considered to be completely demagnetized if the remaining magnetization level is below 10%, due to the pressure distribution in the samples (Figure S4). Zijderveld alternating field demagnetization plots of selected samples labeled ‘3A’, ‘3B’ and ‘3C’ are shown in panels A, B and C of Figure 3, respectively. Vertical lines indicate (magnetic) phase transitions observed in hydrostatic experiments (Ka92 = Kamimura et al., 1992; Ko97 = Kobayashi et al., 1997; LaB = LaBounty et al., submitted; R03 = Rochette et al., 2003).



769

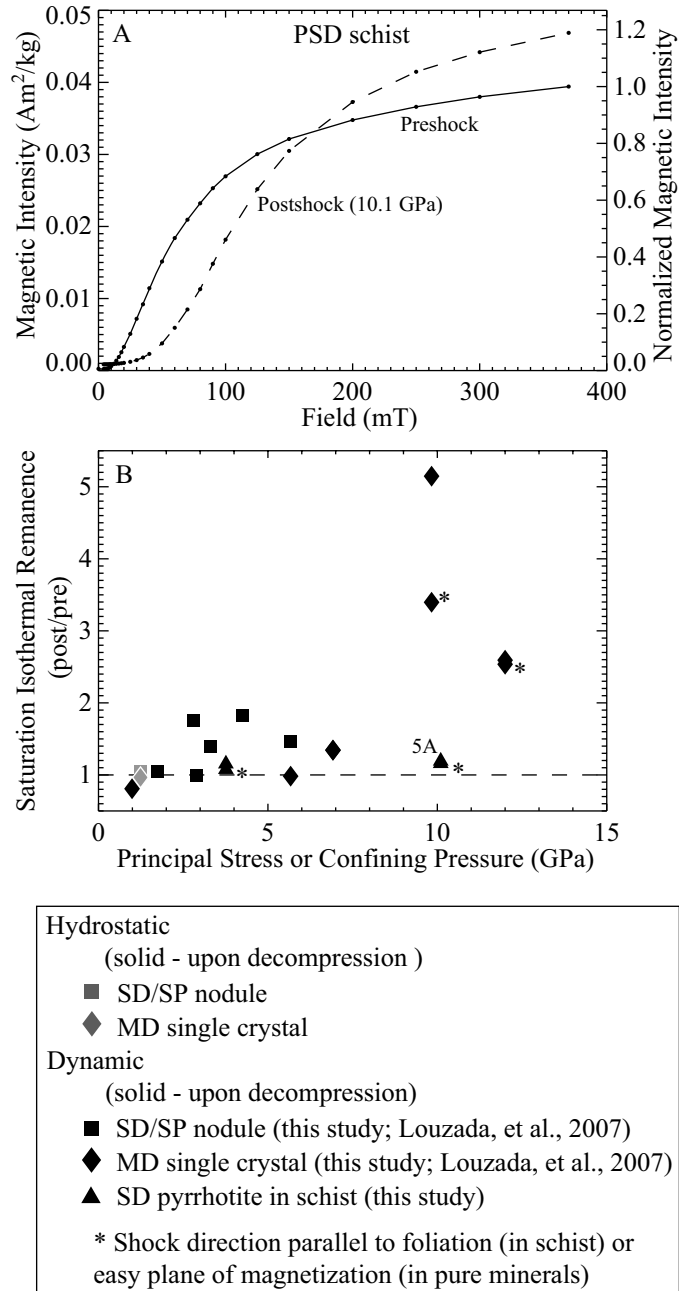
770 **Figure 3** Example orthogonal (Zijderveld) projection plots of alternating field
 771 demagnetization of preshock (saturation isothermal) remanence (black) and postshock remaining
 772 remanence (grey) in specimens of the (A) SD/SP nodule (98080-1D), (B) MD single-crystal
 773 (127037-L), and (C) PSD schist (c4-sa). Squares indicate horizontal projections on the E-N
 774 plane; circles indicate projections on the E-vertical plane. The preshock remanence in the SD/SP
 775 nodule consists of two components, a low coercivity component (LC) removed by peak
 776 alternating fields up to ~15 mT, and a high coercivity component (HC) removed at higher fields.
 777 Pre- and postshock remanence intensities were determined by summing the total vector lengths
 778 (e.g., $|LC|+|HC|$) of the demagnetization plots. A high coercivity component (1-20% of the
 779 saturation remanence) remains in the pyrrhotite-bearing samples upon maximum AF cleaning
 780 (75-95 mT). Numbers indicate peak alternating fields in mT.

781



782

783 **Figure 4** (A) Example alternating field demagnetization curves of the z-component of
 784 preshock remanence (dashed), postshock remaining magnetization (grey) and postshock
 785 resaturation remanence (black) for a SD/SP nodule specimen (98080-1D). MDF_{pre} , MDF_{rm} and
 786 MDF_{post} (extrapolated) are the median destructive fields of the magnetic remanences. (B)
 787 Coercivity spectra of magnetization removed in 1 mT bins of the magnetic remanences derived
 788 from the alternating field demagnetization curves. CSP_{pre} , CSP_{rm} , CSP_{post} are the fields at which
 789 the peaks of the coercivity spectra are located.



790

791 **Figure 5 (A)** An example of saturation isothermal remanent magnetization acquisition curves

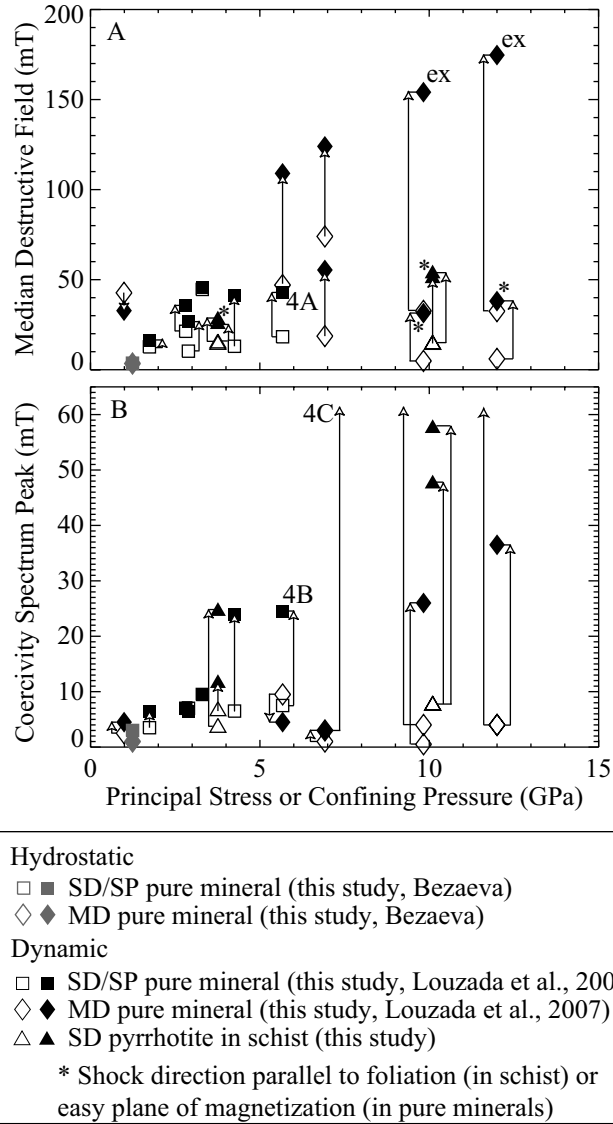
792 up to 380 mT in unshocked (solid) and postshock (9.96 GPa, dashed) PSD schist (c4-sa). The

793 Al2024 capsule makes up 9.7% of the magnetic moment. (B) Change in saturation isothermal

794 remanence of specimens subjected to static and shock compression. Specimen shown in panel A

795 is labeled '5A' in panel B.

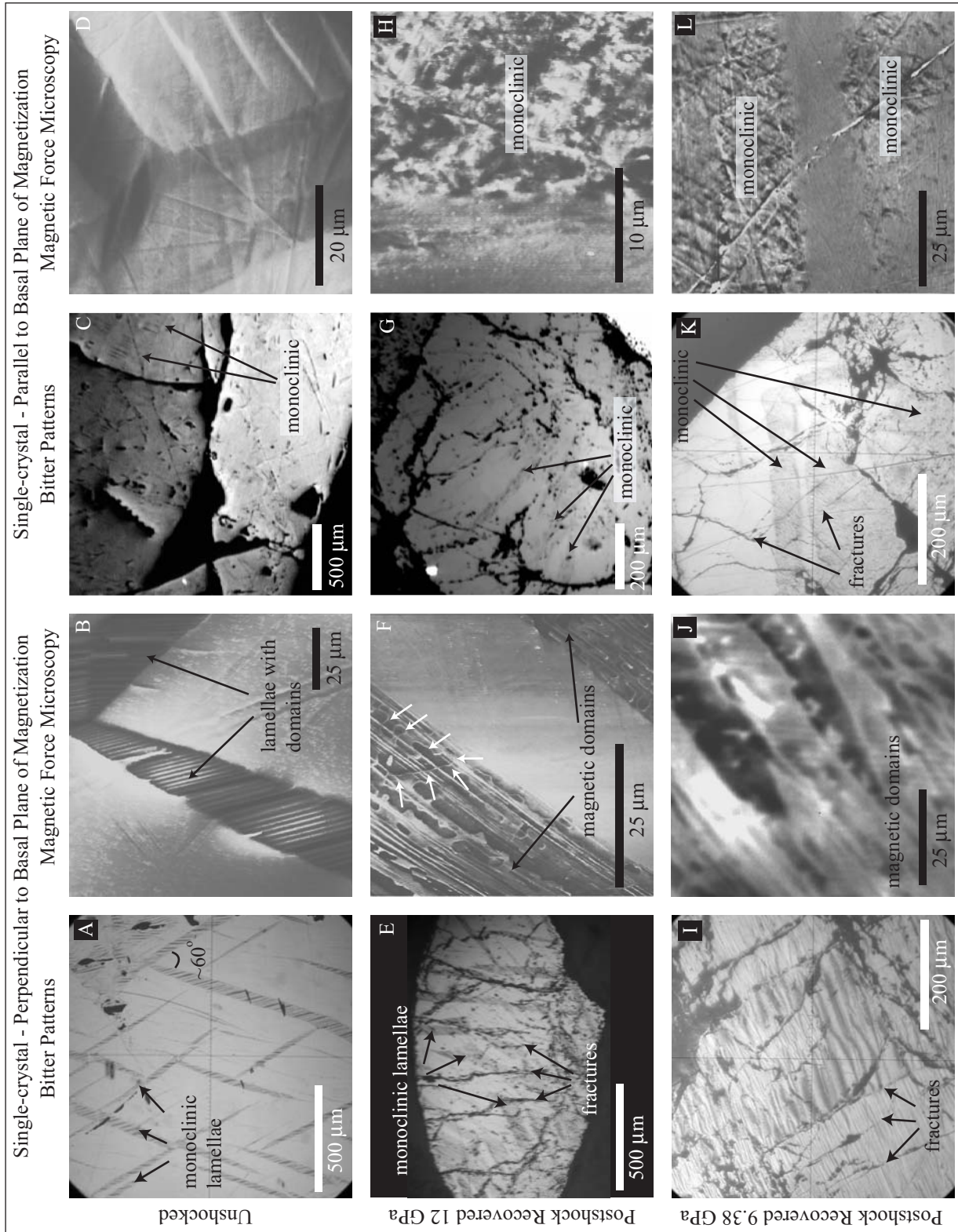
796



797

798 **Figure 6** Pre- (open symbols, MDF_{pre}) and postcompression (solid symbols, MDF_{post})
 799 median destructive fields (MDF) of saturation remanence of static compressed (grey symbols)
 800 and shocked (black symbols) pyrrhotite samples. The postshock MDF of 127037-L and -K were
 801 extrapolated (labeled 'ex'). The grey open and solid symbols are overlapping, indicating no
 802 change in MDF. Example AF demagnetization plots and coercivity spectra are shown in Figures
 803 4A - C, labeled '4A', '4B', and '4C'.

804



805

806

807

808

Figure 7 Magnetic imaging of polished (0.02 μm) (A-D) unshocked and (E-L) postshock recovered MD single-crystal pyrrhotite. Postshock samples are AF demagnetized in 85 mT peak fields. Vertical lines in (J) are an artifact of optical interference.